Phys. Med. Biol. **45** (2000) 933–946. Printed in the UK PII: S0031-9155(00)07912-4

Computed tomography of x-ray index of refraction using the diffraction enhanced imaging method

F A Dilmanian†, Z Zhong‡, B Ren†, X Y Wu†, L D Chapman§, I Orion† and W C Thomlinson‡

† Medical Department, Brookhaven National Laboratory, Upton, NY 11973, USA
‡ National Synchrotron Light Source, Brookhaven National Laboratory, Upton, NY 11973, USA
§ CSRRI, Illinois Institute of Technology, 3301 South Dearborn, Chicago, IL 60616, USA

Received 17 September 1999

Abstract. Diffraction enhanced imaging (DEI) is a new, synchrotron-based, x-ray radiography method that uses monochromatic, fan-shaped beams, with an analyser crystal positioned between the subject and the detector. The analyser allows the detection of only those x-rays transmitted by the subject that fall into the acceptance angle (central part of the rocking curve) of the monochromator/analyser system. As shown by Chapman *et al*, in addition to the x-ray attenuation, the method provides information on the out-of-plane angular deviation of x-rays. New images result in which the image contrast depends on the x-ray index of refraction and on the yield of small-angle scattering, respectively. We implemented DEI in the tomography mode at the National Synchrotron Light Source using 22 keV x-rays, and imaged a cylindrical acrylic phantom that included oil-filled, slanted channels. The resulting 'refraction CT image' shows the pure image of the out-of-plane gradient of the x-ray index of refraction. No image artefacts were present, indicating that the CT projection data were a consistent set. The 'refraction CT image' signal is linear with the gradient of the refractive index, and its value is equal to that expected. The method, at the energy used or higher, has the potential for use in clinical radiography and in industry.

1. Introduction

Diffraction-enhanced imaging (DEI) is a new method of x-ray radiography that was developed in 1995 by Chapman and co-workers (Chapman *et al* 1995, 1997) at the National Synchrotron Light Source (NSLS) for mammography with improved image contrast. DEI uses a fan-shaped, synchrotron-generated x-ray beam, monochromatized by a perfect-crystal monochromator, to measure a subject's x-ray transmission in a line-scan method. The heart of the method is an analyser crystal, typically the same kind as the monochromator's crystal, which is positioned behind the subject in the path of the transmitted beam to the detector. Only the part of the beam transmitted by the subject that satisfies the diffraction condition of the analyser crystal arrives at the detector, which is positioned at the appropriate angle to receive the diffracted photons. The angular yield function of this monochromator/analyser system, which is called the rocking curve, is very narrow (typically several microradians, depending on the crystal and its reflection plane, and on the x-ray energy). Therefore, the efficiency of collecting the transmitted x-rays depends on the out-of-plane angular deviation of the x-ray photons in the fan beam as they traverse the slice of the subject being imaged. In other words, the image contrast is modulated by the shape of the rocking curve and by the angular deviation of the transmitted x-rays out of the fan plane. The net result is an extremely high sensitivity of image contrast to the two physical factors in the tissue that determine this angular deviation (Somenkov *et al*

0031-9155/00/040933+14$30.00

1991, Ingal and Beliaevsky 1995, Davis *et al* 1995): (a) the refraction effect, caused by the out-of-plane gradient of the x-ray index of refraction of the tissue (Yagi *et al* 1999, Arfelli *et al* 1998, Spanne *et al* 1999, Momose *et al* 1999); and (b) the extinction effect, caused by the total cross-section and the angular width of the so-called x-ray small-angle scattering in the tissue (Guinier 1963). Neither of these factors is resolved in conventional radiography (Elleaume *et al* 1999). Radiographs in the planar mode obtained by DEI indicate that the angular sensitivity of the DEI method can be as fine as 0.01 microradians (Chapman *et al* 1997).

The immediate goal of the present work was to answer the following basic questions: (a) Do each of the DEI CT projections constitute a complete set? (b) How complete is the separation of the refraction and apparent absorption images? (c) Will the refractive index signal be linear with the subject's change of refractive index? Our long-term goal is to use DEI CT for characterizing tissues, a necessary step in evaluating the potential of the DEI method in clinical radiography both in the planar mode for mammography and in the CT mode for whole-body imaging. Tissue characterization in the planar mode of a complex sample is virtually impossible because of the interference of overlying tissues.

2. Theory

In a DEI experiment, a fan beam of monochromatic x-rays is generated by a double-bounce, perfect-crystal monochromator. This beam then traverses the sample and is diffracted by an analyser crystal to the extent that it satisfies the angle-energy condition. The angular deviation of x-ray photons from their original direction can be caused either by their crossing boundaries between tissues with different refractive indices, or by small-angle scattering. For a horizontal incident beam, these vertical deviations, $\Delta\theta_z$, are typically on the order of 10^{-6} radians. When the analyser is tuned to the shoulder of the rocking curve (figure 1), this angular deviation changes the intensity ΔI of the x-rays diffracted by the analyser crystal (and thus reaching the detector), producing an image contrast. The resulting modulation of image contrast depends on the angular width of the analyser's rocking curve, and on the position on the rocking curve to which the analyser is tuned, besides the amount of angular deviation itself.

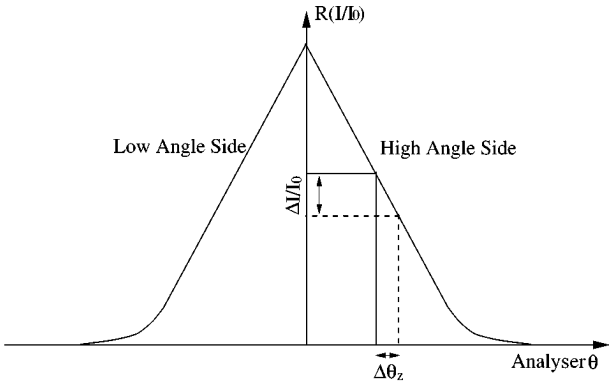

Figure 1. Principles of DEI.

As discussed, angular deviations are caused by variations in the refractive index and by small-angle scattering. The response of the method to these two effects differs. The index-of-refraction effect is directional, i.e. toward above- or below-the fan plane angles (that is, to

the right or to the left direction on the abscissa of figure 1), while small-angle scattering is symmetric above and below the plane. This difference allows these effects to be separated from each other, and from 'gross attenuation', by acquiring images of the subject at the symmetrical points on the rocking curve (Chapman *et al* 1997). As described below, the refractive index can be separated quite well from the effects of small-angle scattering (when the preponderance of the latter is not significant) and from gross attenuation, by subtracting the high- and low-angle images with appropriate normalization factor. Similarly, small-angle scattering present in the 'gross attenuation' image can be suppressed by adding the high- and low-angle images with an appropriate normalization factor, producing an 'apparent absorption' image. The magnitude of apparent absorption is larger than that for gross attenuation because the small-angle scattering is removed; the effect is called the 'extinction effect' (Chapman *et al* 1998). Extinction can also be observed by acquiring an image at the sharp peak of the rocking curve (figure 1); although this 'top' image includes some refractive index effect, it has the important advantage over the apparent absorption image in that it does not suffer from the additional image noise caused by image addition and subtraction. This paper concentrates on the refractive-index effect.

Detecting the refraction contrast requires the analyser's rocking curve to have an extremely small angular width. This width is characterized by the Darwin width W_D of perfect-crystal diffraction (Batterman and Cole 1964). For hard x-rays (i.e. 20–70 keV), which have a good transmission through thick body sections, the rocking-curve width of a perfect silicon crystal is around 1 to 10 microradians, depending on the energy and the order of crystal diffraction.

The refraction angle, $\Delta\theta_z$, is defined as the angle in the plane of diffraction by which the x-rays deviate from the original direction while traversing the sample (Chapman *et al* 1997). Assuming there is no significant effect of small-angle scattering, $\Delta\theta_z$ can be derived by measuring the intensity of the x-rays transmitted through the sample and then diffracted by the analyser, with the analyser tuned to the shoulders of the rocking curve, once at the high-angle side, θ_H, and once at the low-angle side, θ_L (figure 1). $\Delta\theta_z$ is given by

$$\Delta\theta_z = \frac{I_H R_{\theta_L} - I_L R_{\theta_H}}{I_L(\mathrm{d}R/\mathrm{d}\theta)_{\theta_H} - I_H(\mathrm{d}R/\mathrm{d}\theta)_{\theta_L}} \tag{1}$$

where I_H and I_L are the intensities measured with the analyser at θ_H and θ_L respectively, $R(\theta)$ is the height of the rocking curve at the analyser position θ, and $(\mathrm{d}R/\mathrm{d}\theta)_{\theta_H}$ and $(\mathrm{d}R/\mathrm{d}\theta)_{\theta_L}$ are the slopes of the rocking curves at θ_H and θ_L respectively.

When an x-ray beam passes through a non-homogeneous medium, the propagation of the beam follows (Synge 1962):

$$\frac{\mathrm{d}}{\mathrm{d}l}(n\boldsymbol{i}) = \nabla(n) \tag{2}$$

where $\boldsymbol{i}$ is the unit vector tangent to the ray's path, l is the position along the path in the sample and n is the refractive index. For x-rays, n is slightly smaller than unity. Thus

$$n\frac{\mathrm{d}\boldsymbol{i}}{\mathrm{d}l} = \nabla(n) - \frac{\mathrm{d}n}{\mathrm{d}l}\boldsymbol{i}. \tag{3}$$

It can be further shown that for a horizontal ray path, as in our experiment, the angular deviation of the beam in the vertical direction is proportional to $\partial n/\partial z$. Therefore, the line integration of these deviation along the path of the beam is

$$\Delta\theta_z = \int \frac{\partial n}{\partial z}(l)\,\mathrm{d}l. \tag{4}$$

For two CT projections taken at the same angular position of the subject but on both sides of the rocking curve, the overall $\Delta\theta_z$ value can be obtained on a pixel by pixel basis using equation (1). These $\Delta\theta_z$ values are then used to create a refraction-angle sinogram.

Furthermore, since equation (4) is similar in form to the usual line integrals used in sinograms in normal CT, filtered back-projection (FBP) algorithms can be used to reconstruct CT images. Such images would be maps of the distribution of the z-gradient of the refractive index, $\partial n/\partial z(x, y)$, in the sample.

The refractive index is related to the number density of electrons in the material in the following way:

$$n = 1 - \frac{1}{2\pi} r_e N \lambda^2 \tag{5}$$

where N is the number of electrons per unit volume of the sample material, r_e is the classical radius of the electron and λ is the x-ray wavelength. Thus, the refractive index gradient is a physical factor, different from the absorption of x-rays, that can produce pure image contrast of its own in clinical DEI images.

3. Experimental method

Figure 2 shows the set-up of the DEI at beamline X15A. The monochromator and analyser are both positioned on a granite block, 0.375 m wide, 0.3 m tall and 2.1 m long. The block is isolated from vibrations of the floor by rubber pads and vibration-insulating composite plates placed under the legs of the steel frame that supports the block (Mangra *et al* 1996). The monochromator is positioned inside a steel tank, sitting on the granite block and mechanically isolated from the beamline pipe by an air gap of 2 cm. To reduce the rate of ozone production, the lower part of the x-ray spectrum (with energy less than 13 keV) is essentially eliminated using a 1 mm thick aluminium filter positioned downstream of the beamline's beryllium window. The aluminium filter attenuates the 22 keV x-rays by only about 50%. The sample-scanning stage and shutter are placed on a platform positioned on a second steel frame which is directly supported by the floor. Thus, the stage and the shutter are isolated from the granite block.

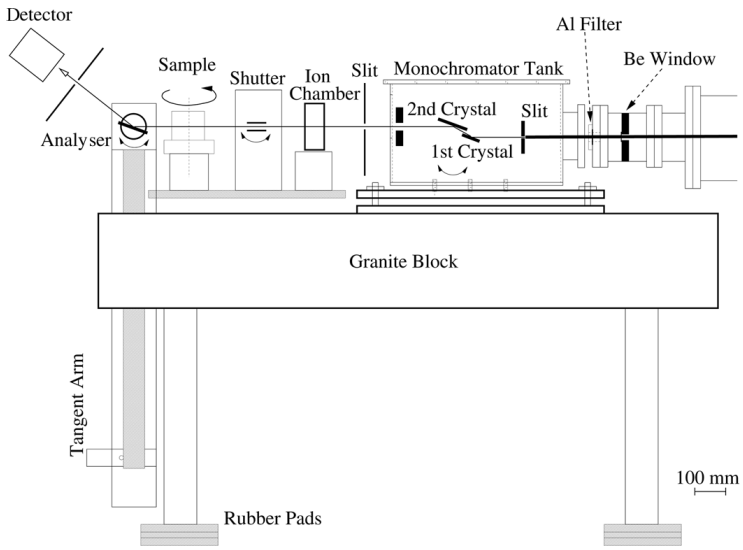

Figure 2. Set-up at the NSLS X15A beamline.

3.1. The x-ray source

X15A is a standard NSLS bending-magnet beamline. The fan beam is 130 mm wide at the entrance to the experimental hutch, which is 16.3 m from the source. The useful height of the fan beam is about 2 mm (i.e. when the intensity falls 20% below the flat top).

The aperture of the fan beam used for the experiment was 1.7 mm high and 128 mm wide. The x-ray storage ring operated at 2.800 GeV energy. The maximum ring current was 230 mA.

3.2. Monochromator and analyser system, and the monochromatic beam

The monochromator/analyser system was that developed by Thomlinson and colleagues (Chapman *et al* 1998, Thomlinson *et al* 1998, Zhong *et al* 1999) for DEI in the planar mode. It employed a two-crystal, fixed exit, Bragg–Bragg monochromator using either a silicon [111] or [333] reflection, and another Bragg silicon crystal of the same reflection as the analyser. The [111] and [333] reflections were chosen for comparison because of a five-fold difference in the widths of their rocking curves. The monochromator was placed inside the stainless steel tank with helium at atmospheric pressure to prevent corrosion of its components by ozone. The system was constantly purged with helium at a flow rate of 50 $cm^3\ min^{-1}$. Each crystal was 10 mm thick and 150 mm wide, with strain relief cuts (2 mm wide and 8 mm deep) at 10 mm from the ends of the crystal. Thus, the useful width of the crystal was 128 mm. The first crystal was 60 mm long along the beam's direction, and the second one was 90 mm. The large length of the second crystal allowed a long range of energy change without requiring adjustment of the distance between the two crystals. For example, in the [333] mode, the energy of the monochromator could be changed from 15 keV to 65 keV simply by adjusting the angle of the crystal.

The monochromator is a box-type design with a vertical offset of 1 cm between the two crystals (Zhong *et al* 1999). The first and second crystals are mounted on the bottom and top plates of the box respectively. Each crystal is mounted on kinematic mounts for adjusting the Bragg and azimuthal angles, and is supported on the back side by three balls placed under the strain-relief region, and secured on the front side by clamps. The box is mounted on a cradle, so that the middle of the first crystal surface is at the centre of rotation. Because of its simplicity, the box-type design is especially resistant to vibration. The instability of the beam's horizontal profile was 0.2% min^{-1}, after the monochromator crystals reached thermal equilibrium. This instability was assumed to be caused by mechanical or thermal drifts. The thermal equilibrium was reached in about 5 min after the white beam was first put on the monochromator's crystal.

The analyser crystal is of the same kind as the second crystal of the monochromator. The crystal's Bragg angle is controlled by a tangent arm of length 1 m, driven by a linear translator of resolution 0.1 μm. This arrangement provides an angular resolution of 0.1 microradians, which allows the analyser to be tuned at a precision angle equal to 1/30th of the full-width at half-maximum (FWHM) of the rocking curve. The tangent arm is supported by the same granite block that supports the monochromator.

The results presented here were obtained at 22 keV. Figure 3 shows the [111] and [333] rocking curves of the analyser crystal at this energy. The curve's FWHM is approximately 3 microradians for the [333] reflection, and 15 microradians for the [111] reflection. The intensities of the monochromatic beam at the subject for these two reflections were 5.8×10^9 and 9.2×10^{10} photons/s/cm^2 respectively at a ring current of 200 mA. The total amount of beam harmonics for Si[333] (i.e. 29.3 keV caused by [444] reflection, and 36.6 keV caused by [555] reflection) was estimated to be around 20%, while that for Si[111] was negligible.

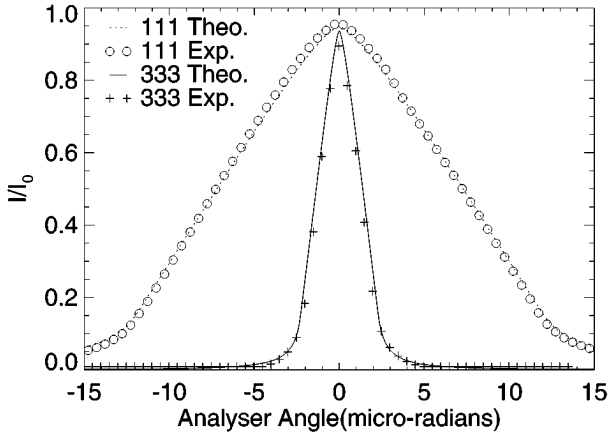

Figure 3. Theoretical and measured analyser rocking curves at 22 keV of Si [111] and [333] reflections.

3.3. Detector and data acquisition system

The detector and the data acquisition system (DAS) were those of the program Multiple Energy Computed Tomography (MECT) (Dilmanian *et al* 1991, 1997), a monochromatic beam computed-tomography system which was developed at the NSLS's X17B beamline. The detector, a linear-array device with a 0.92 mm pitch, employed a $CdWO_4$ scintillator array developed by Harshaw-Bicron (Solon, Ohio), and a photodiode array developed by Hamamatsu (Hamamatsu City, Japan). It was designed and integrated by Analogic Corporation (Peabody, MA). The DAS, which was also developed by Analogic Corporation, operated at 1440 Hz viewing rate. To improve the image's spatial resolution, the detector was masked by a tantalum grid that limited the active width of each element to one-half of the detector's pitch, i.e. 0.46 mm.

3.4. The subject

The subject was a 50.8 mm diameter acrylic cylindrical phantom that included four non-paraxial, oil-filled cylindrical channels. Figure 4 shows the design of the phantom. It was imaged transaxially as it rotated approximately about its axis. The diameters of the channels and their tilt angles with respect to the phantom axis were the following: (a) 12.7 mm and 10 degrees; (b) 9.53 mm and 10 degrees; (c) 9.53 mm and 5 degrees; and (d) 9.53 mm and 15 degrees. The channels were filled with olive oil to avoid small bubbles forming on the walls of the channels that were produced when the channels were filled with water.

3.5. Types of measurement

A DEI scan is done by fixing the analyser at a specific angle and rotating the sample through 360° while the projection data are acquired. Three sets of projections were acquired from the same sample with the analyser's angle tuned to $-W_D/2$, $W_D/2$ and 0, where W_D is the FWHM of the rocking curve.

At each location on the analyser's rocking curve, four sets of CT image projections, of 360° each, were acquired at consecutive lateral shifts of 0.23 mm (with respect to the beam) of the subject's axis of rotation. The stage rotated at the rate of 15 s per complete turn. The four data sets were interlaced during image reconstruction to improve the spatial resolution.

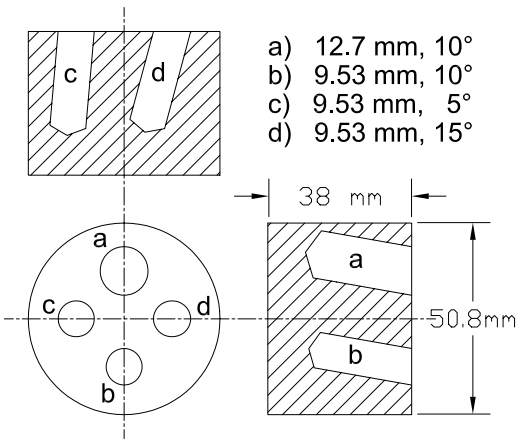

Figure 4. Design of the phantom.

Since the width of the rocking curves was about 3.0 and 15 microradians for the two crystal planes, the data were taken once at an analyser angle of 0.0 and then at ± 1.5 microradians for [333] and ± 7.5 microradians for [111]. For comparison with the DEI images, a normal CT was performed by removing the analyser crystal and positioning the detector in the path of the beam through the sample.

All scans were controlled by a DEC Alpha computer with a program specifically written for the CT experiment. The program obtains from the user data such as the type of scan and the analyser positions. It then performs the scan by controlling the stepper motors that rotate and shift (lateral to the beam) the sample. The program also acquires readings from the ion chamber current throughout the scan to measure the dose.

4. Results

4.1. Data analysis

Figures 5(*a*)–(*c*) show the CT reconstructions of the direct measurements with the analyser tuned to the left shoulder, top of the peak and the right shoulder of the rocking curve for Si[333] respectively. Figures 6(*a*)–(*c*) are similar to figures 5(*a*)–(*c*) except that the data are for Si[111]. Figures 5(*d*) and 6(*d*) show the normal CT images taken at the same 22 keV energy, with Si[333] and Si[111] reflections respectively. Two effects are clear from these pictures: first, the refraction signals change sign as one switches from one shoulder of the rocking curve to the other. Second, the refraction signal in the top images is very small, and that is spread equally on both sides of the channels; any asymmetry between the two oppositely positioned signals could have been caused by a one-sided drift of the analyser during data acquisition. As was discussed in section 2, the top images have great similarity to the apparent absorption images in that in both image types the refraction signal is almost absent and, more importantly, small-angle scattering is suppressed. On the other hand, the image noise is much smaller in the top images because they are direct images, not compound ones, with the count statistics twice as big as the individual components that make the apparent absorption images. In the experiments, θ_L and θ_H were symmetrical points on both sides of the rocking curve, thus $(\mathrm{d}R/\mathrm{d}\theta)_{\theta_H} = -(\mathrm{d}R/\mathrm{d}\theta)_{\theta_L}$. Since $\theta_H = W_D/2$ and $\theta_L = -W_D/2$,

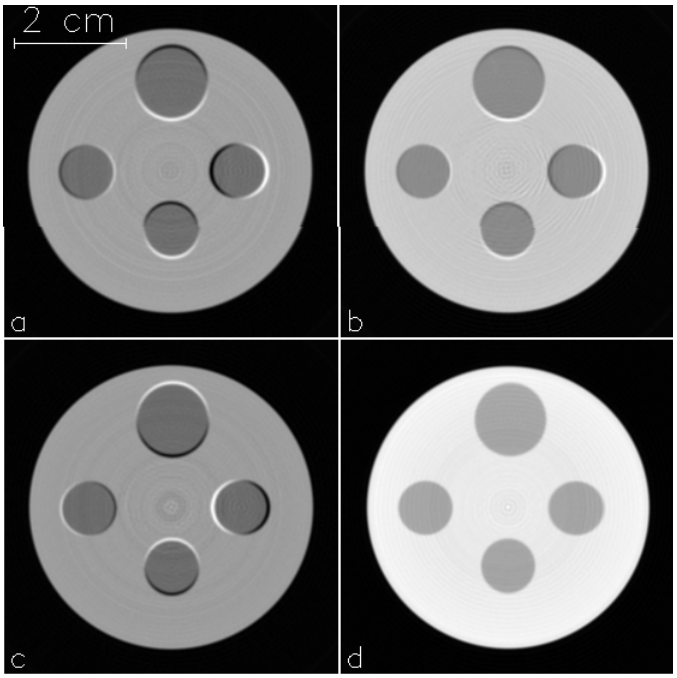

Figure 5. Images of the slanted-channel phantom obtained using the Si[333] monochromator and analyser at 22 keV, with the analyser at (*a*) −1.5 microradians, (*b*) the peak of the rocking curve and (*c*) +1.5 microradians; (*d*) is the normal CT image taken by removing the analyser crystal, with the two-crystal monochromator tuned to the peak intensity.

Table 1. Peak values (in units of 10^{-7} cm^{-1}) at the inner and outer edges of the oil channels in the refraction images.

Channel	Slant angle (deg)	[111]	[333]
c	5	−2.1, +2.1	−0.82, +1.4
a	10	−3.9, +3.5	−2.4, +2.9
b	10	+3.6, −3.6	+2.3, −2.7
d	15	+4.7, −5.0	+3.6, −3.8

then $R(\theta_L) = R(\theta_L) = R_p/2$, where R_p is the peak reflectivity of the analyser. Under these conditions, equation (1) is reduced to

$$\Delta\theta_z = \frac{R_p}{2(\mathrm{d}R/\mathrm{d}\theta)_{-W_D/2}} \frac{I_H - I_L}{I_H + I_L}. \tag{6}$$

During off-line image reconstruction, first, each 24 adjacent views in each data set were combined to produce a sinogram of 900 projections over 360°. Next, the four shift sets were combined in one sinogram. Finally, equation (6) was used to generate a refraction-angle sinogram. The FBP method then was applied to produce CT images of the z-gradient of the refractive index, $\partial n/\partial z(x, y)$. In reconstructing the CT images, we used a Hanning filter with 0.5 cut-off frequency.

Figures 7(*a*) and (*b*) show the processed images with Si[333]: (*a*) refraction image and (*b*) apparent absorption image; figures 8(*a*) and (*b*) show the same for Si[111]. The in-plane spatial resolution in these images is about 0.3 mm. The peak pixel values at the inner and

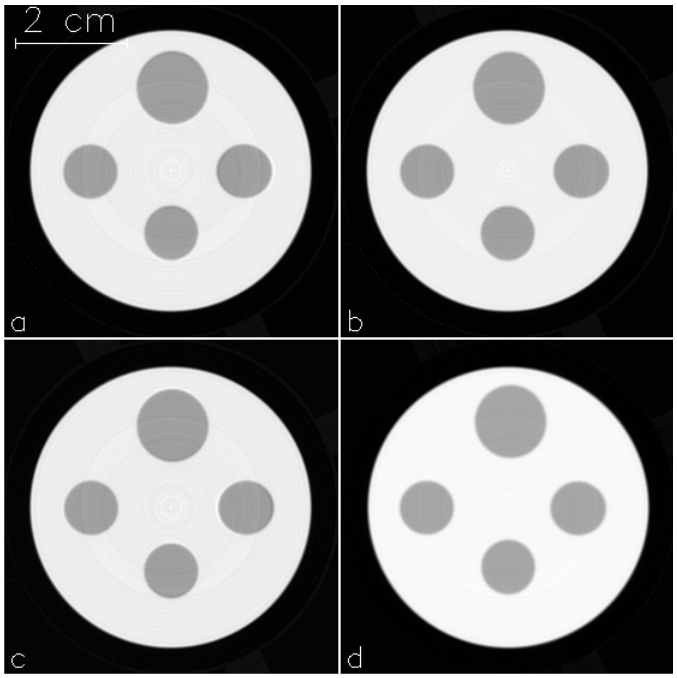

Figure 6. Images of the slanted-channel phantom obtained using the Si[111] monochromator and analyser at 22 keV with the analyser at (*a*) −7.5 microradians, (*b*) the peak of the rocking curve and (*c*) +7.5 microradians; (*d*) is the normal CT image taken by removing the analyser crystal.

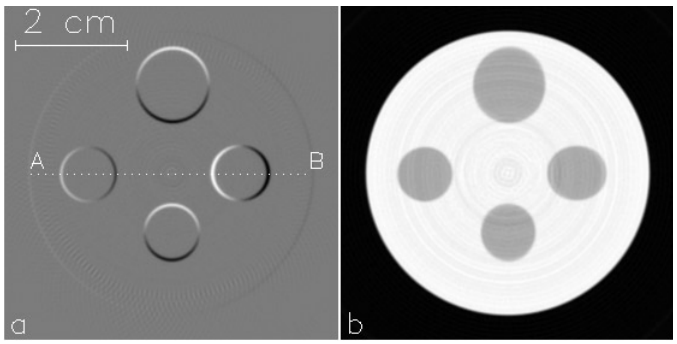

Figure 7. Images of the slanted-channel phantom obtained at 22 keV with Si[333] monochromator and analyser: (*a*) refraction image and (*b*) apparent absorption image.

outer edges of the four oil channels (along the phantom's radii) are shown in table 1 for both reflections. The image background was $(0.0 \pm 1.8) \times 10^{-8}$ cm^{-1} and $(0.0 \pm 5.9) \times 10^{-9}$ cm^{-1} for Si[333] and Si[111] respectively. For a 5° tilt angle, the signal-to-noise ratios are 12 and 19 for Si[333] and Si[111] respectively.

4.2. Characterization of refraction

In the following mathematical analysis, the expected signal size in the refraction images is calculated. We first assume that the spatial resolution of the image and the pixel size are

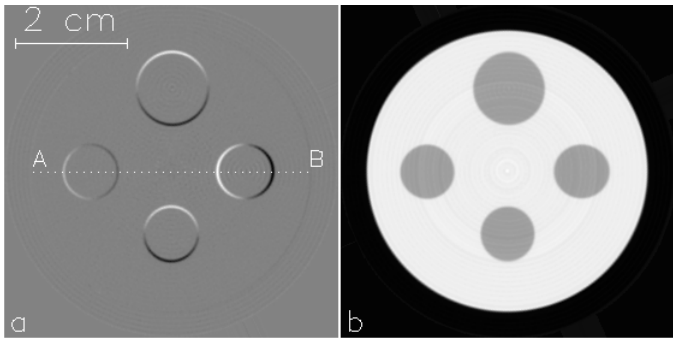

Figure 8. Images of the slanted-channel phantom obtained at 22 keV with Si[111] monochromator and analyser: (*a*) refraction image and (*b*) apparent absorption image.

infinitely small. To relate the image signals to the actual refractive index gradients, we use equations (1) and (4) to produce $\Delta\theta_z$ images, and compare the signal in the image with $\Delta\theta_z$ derived from the properties of the phantom as described below. We denote the refractive indices of acrylic and oil as n_1 and n_2 respectively. Thus, $\partial n/\partial z(l)$ is zero except at the interface between the oil and acrylic at the edges of the slanted channels. For an infinitely thin vertical beam-height, the signal will be

$$\frac{\partial n}{\partial z}(l) = (n_2 - n_1)\tan\theta\,\delta(l - l_0) \tag{7}$$

where θ is the tilt angle of the channel, $\delta(l - l_0)$ is a delta function and l_0 is the location of the intercept between the beam and the channel wall. For a finite vertical beam height of h, the width Δl of the profile of the refraction image is given by

$$\Delta l = h\tan\theta. \tag{8}$$

The area under the peak is given by

$$A = \int_{l_0+\Delta l/2}^{l_0-\Delta l/2} \frac{\partial n}{\partial z}(l)\,\mathrm{d}l = (n_2 - n_1)\tan\theta. \tag{9}$$

Since the electron number density is proportional to the density for most materials, equation (5) can be approximated by (Guinier 1963)

$$1 - n \cong 1.3 \times 10^{-6}\rho\lambda^2 \tag{10}$$

where ρ is the density of the material in g cm^{-3} and λ is the x-ray wavelength in Å. Equation (9) then becomes

$$A \cong 1.3 \times 10^{-6}\lambda^2\tan\theta(\rho_1 - \rho_2). \tag{11}$$

Equation (11) holds for digital images of finite pixel size and throughout the CT reconstruction process because both the digitization of the image (i.e. binning of the content of the space) and the FBP process are linear mathematical processes. In particular, the FBP involves a set of linear image processing steps (Rosenfeld and Kak 1982) that do not change the validity of equation (9). These steps include (a) division of the CT image plane into square segments that define the pixels, (b) for each projection, convolution of the data with a fixed, linear filter, and (c) for each projection, back-projection of each data point across the CT image plane. The latter step involves allocating counts to each pixel according to the overlap of the areas of the square pixel and the back-projecting ray.

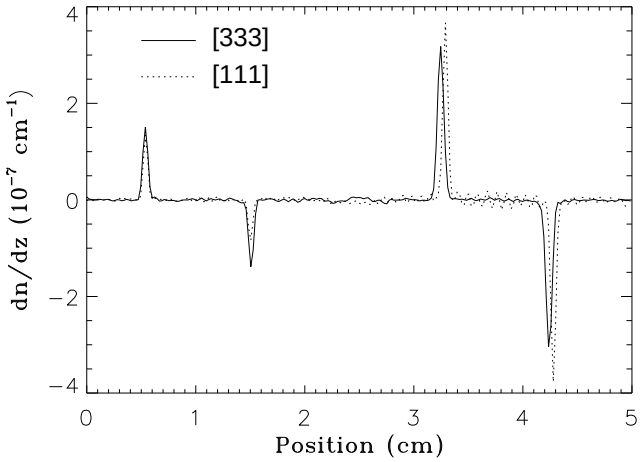

Figure 9. Line profiles through the centre of the Si [333] and [111] refraction images, crossing the 5° and the 15° channels.

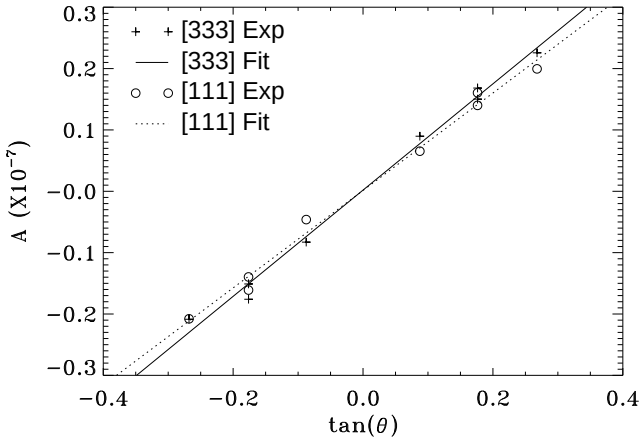

Figure 10. Area under the peak versus the phantom's channel slope for Si[333] and [111].

Line profiles through the centre of the refraction image (along line AB in figures 7(*a*) and 8(*a*), crossing the 5° and the 15° channels) are shown in figure 9. From this and similar other profiles, quantitative information was deduced about the refraction signals at the edges of the titled channels. These data included peak pixel value and the total area underneath each peak.

Figure 10 shows the area A under the peaks in figure 9 at 22 keV versus the tangent of the channel tilt angle θ for Si[333] and Si[111] analysers. The full curves are the linear least-square fitting of the data. Within experimental error, the area is proportional to the slope of the phantom channel. The slope of the fitted line in figure 10 is 8.6×10^{-8} for Si[333] and 8.0×10^{-8} for Si[111]. These values agree rather well with the theoretical value $(n_2 - n_1)$ of 9.1×10^{-8} calculated (equations (9) and (11)) using the measured specific gravities of 1.16 and 0.9088 g cm^{-3} for acrylic and olive oil, respectively.

Table 2. Attenuation coefficients for oil and acrylic in the apparent absorption and in normal CT, in units of cm^{-1}.

Reflection	Material	Apparent absorption	Normal CT	Apparent absorption/normal CT
[333]	Oil	0.35	0.32	1.11
	Acrylic	0.52	0.45	1.16
[111]	Oil	0.36	0.36	1.00
	Acrylic	0.55	0.55	1.00

4.3. Comparing images of apparent absorption and normal CT

As discussed, the apparent absorption (I_r) image is obtained by adding the images from the opposite sides of the rocking curve. In a process parallel to that which leads to equation (1), we obtain

$$I_r = \frac{I_L(\mathrm{d}R/\mathrm{d}\theta)_{\theta_H} - I_H(\mathrm{d}R/\mathrm{d}\theta)_{\theta_L}}{R(\theta_L)(\mathrm{d}R/\mathrm{d}\theta)_{\theta_H} - R(\theta_H)(\mathrm{d}R/\mathrm{d}\theta)_{\theta_L}}. \tag{12}$$

The resulting image should be similar to the normal CT image, except for the 'extinction' effect, i.e. suppression of the small-angle scattering effect.

For the Si[333] experiment, comparing the apparent absorption image (figure 7(*b*)) with the normal CT image (figure 5(*d*)), we find that not only are the image values for oil and acrylic different in these two image types, but their ratios are also different. However, the Si[111] results are almost identical for these two image types. The results are summarized in table 2.

The difference between the oil/acrylic contrast ratios, measured once in normal CT and once in apparent absorption CT in the Si [333] geometry, is mainly due to a small content (10–20%) of beam harmonics in the normal CT beam (Zhong *et al* 1999). Such an effect is absent from the apparent absorption CT image because when a monochromator is 'detuned' (i.e. shifted from its peak yield, such as is the case in the geometries at which the 'left' and 'right' images are acquired) the beam harmonics are significantly suppressed (Hart and Berman 1998). On the other hand, the Si [111] experiment does not have any beam harmonics, neither in the conventional images nor in the apparent absorption CT images, because the first beam harmonic of Si[111] is at three-fold the fundamental beam energy, i.e., 66 keV in our experiment, at which the spectral yield of the beam line of XISA falls to negligible values. On the other hand, the [444] and [555] harmonics in the Si [333] geometry are of energy 29.3 keV and 36.7 keV, and their yields are estimated to be 10–20% at the tuned and less than 1% at the detuned position (Zhong *et al* 1999). The evidence for the existence of beam harmonics in the Si[333] configuration is that the contrast of the acrylic (normalized to that of oil) is smaller in the normal CT than in the apparent absorption CT image; this difference is due to the fact that the high-energy component of the beam (i.e. beam harmonics) in the normal CT image lowers the mean attenuation coefficient of the subjects with a higher mean atomic number (i.e. acrylic versus oil). Existence of beam harmonics also explains another effect: among the directly obtained images in the Si [333] experiment, i.e. the 'left', 'top', 'right' as well as the normal CT images (figures 5(*a*)–(*d*)), those that are supposed to have beam harmonics ('top' and normal CT images) exhibit a distinct cupping effect (not shown), which is characteristic of a polychromatic beam CT; such an effect is absent from the 'left' and 'right' images where the analyser was detuned, therefore rejecting harmonics.

The arguments discussed above do not exclude the possibility that there is also a component of the 'extinction' effect in the image-contrast ratios of the Si [333] results in table 2, which is missing from the Si [111] results. However, theoretical considerations indicate that such components must be small because both olive oil and acrylic plastics are essentially homogeneous materials with no internal structures, and the 'extinction' effect stems from

Table 3. The oil and acrylic attenuation coefficients from all images with the [111] and [333] analysers. The 'signal' is defined as the difference of the acrylic and oil absorption coefficients. The image noise is the value of standard deviation in the acrylic image. SNR is the signal-to-noise ratio.

Reflection	Image	Oil (cm^{-1})	Acrylic (cm^{-1})	Signal (cm^{-1})	Noise (cm^{-1})	SNR
[333]	Left	0.352	0.517	0.165	0.0052	32
	Right	0.352	0.518	0.166	0.0060	28
	Top	0.322	0.460	0.138	0.0039	36
	Normal CT	0.319	0.447	0.129	0.0032	40
	Apparent absorption	0.353	0.518	0.164	0.0045	36
[111]	Left	0.366	0.550	0.185	0.0034	54
	Right	0.366	0.550	0.184	0.0033	55
	Top	0.365	0.550	0.185	0.0030	62
	Normal CT	0.365	0.550	0.185	0.0021	87
	Apparent absorption	0.366	0.550	0.184	0.0033	56

materials which have a structural variation with a length scale of microns, such as muscles or other fibrous materials.

4.4. Comparing of image noises in different images

Table 3 summarizes the attenuation coefficients of oil and acrylic in all images for both [111] and [333] reflections. It also summarizes the noise in these images. We note that the apparent absorption images, being compound images made from low-count components, have small signal-to-noise ratios (SNR), while the top images and normal CT have the largest.

We note that the image noise in all these pictures is above 10 Hounsfield units (HUs), compared with 1–3 HU in clinical CT. This effect, considering the doses to the phantom (190 rad for [111] and 10 rad for [333]), is mostly attributed to the high spatial resolution in our images, approximately 0.3 mm in-plane and 1.5 mm out-of-plane FWHM, compared with typical values of 0.6 mm in-plane and 5 mm out-of-plane in conventional CT.

5. Discussion

From our study we draw the following conclusions:

(a) DEI CT projections are complete sets, and thus can be reconstructed conventionally.
(b) The separation of the refraction image from the other image components is complete for material with little small-angle scattering, such as oil and acrylic.
(c) The image contrast is proportional to the gradient of the refractive index.
(d) There is a remarkable agreement between the linearity trends of the experimental findings and the theoretical refractive index results. The absolute values agree within 20%.

The refraction signal declines only as the inverse function of the x-ray energy. Therefore, we expect that x-ray beams of much higher energy (i.e. 60–90 keV) could still be used for this type of CT imaging. In particular, clinical application of the refraction image in DEI CT would be one of edge enhancement, and may find various uses in medicine. It is also possible that the method will find industrial applications in non-destructive testing.

Acknowledgments

We thank Betsy Dowd, Dale Sayers, Peter Siddons, Gerry Vanderlaske and Avril Woodhead for assistance. This research was supported by a Laboratory Directed Research and Development (LDRD) grant from BNL which is, in turn, supported by the US Department of Energy under the contract DE-AC02-CH10886.

References

Arfelli F *et al* 1998 Low-dose phase contrast x-ray medical imaging *Phys. Med. Biol.* **43** 2845–52

Batterman B W and Cole H 1964 Dynamical diffraction of X rays by perfect crystal *Rev. Mod. Phys.* **36** 681–717

Chapman D, Pisano E, Thomlinson W, Zhong Z, Johnston R E, Washburn D and Sayers D 1998 Medical and biological applications of diffraction enhanced imaging *Breast Disease* **10** 197–207

Chapman D, Thomlinson W, Arfelli F, Gmür N, Zhong Z, Menk R, Johnston R E, Washburn D, Pisano E and Sayers D 1995 Mammography imaging studies using a laue crystal analyzer *Rev. Sci. Instrum.* **67** (CD suppl)

Chapman D, Thomlinson W, Johnston R E, Washburn D, Pisano E, Gmür N, Zhong Z, Menk R, Arfelli F and Sayers D 1997 Diffraction enhanced x-ray imaging *Phys. Med. Biol.* **42** 2015–25

Davis T, Gao D, Gureyev T, Stevenson A W and Wilkins S W 1995 Phase-contrast imaging of weakly absorbing materials using hard x-rays *Nature* **373** 595–8

Dilmanian F A *et al* 1991 Computed tomography with monochromatic x-rays from the National Synchrotron Light Source *Nucl. Instrum. Methods* B **56/57** 1208–13

Dilmanian F A *et al* 1997 Single- and dual-energy CT with monochromatic synchrotron x-rays *Phys. Med. Biol.* **42** 371–87

Elleaume H *et al* 1999 Instrumentation of the ESRF medical imaging facility *Nucl. Instrum. Methods Phys. Res.* A **428** 513–27

Guinier A 1963 *X-ray Diffraction in Crystals, Imperfect Crystals and Amorphous Bodies* (San Francisco: Freeman) section 1.1

Hart M and Berman L 1998 X-ray optics for synchrotron radiation; perfect crystals, mirrors and multilayers *Acta Crystallogr.* A **54** 850–8

Ingal V N and Beliaevsky E A 1995 X-ray plane-wave topography observation of phase contrast from a non-crystalline object *J. Phys. D: Appl. Phys.* **28** 2314–17

Mangra D, Sharma S and Jendrzejczyk J 1996 Passive vibration damping of the APS machine components *Rev. Sci. Instrum.* **67** 3374

Momose A, Yoneyama A, Takeda T, Itai Y, Tu J and Hirano K 1999 Project for application of phase-contrast x-ray imaging to medicine using an x-ray interferometer *Proc. SPIE* **3770** 23–31

Rosenfeld A and Kak A C 1982 *Digital Picture Processing* 2nd edn (San Diego: Academic) pp 353–430

Somenkov V A, Tkalich A K and Shil'shtein S 1991 Refraction-contrast in x-ray introscopy *Sov. Phys. Tech. Phys.* **36** 1309–11

Spanne P, Raven C, Snigireva I and Snigirev A 1999 In-line holography and phase-contrast microtomography with high energy x-rays *Phys. Med. Biol.* **44** 741–9

Synge J L 1962 Geometrical optics *Cambridge Tracts in Mathematics and Mathematical Physics* No 37, ed F Smithies and J A Todd (Cambridge: Cambridge University Press) p 102

Thomlinson W, Chapman D, Zhong Z, Johnston R and Sayers D 1998 Diffraction enhanced x-ray imaging *Medical Applications of Synchrotron Radiation* ed M Ando and C Uyama (Tokyo: Springer) pp 72–7

Yagi N, Suzuki Y, Umetani K, Kohmura Y and Yamasaki K 1999 Refraction-enhanced x-ray imaging of mouse lung using synchrotron radiation source *Med. Phys.* **26** 2190–3

Zhong Z, Thomlinson W, Chapman D and Sayers D 1999 Implementation of diffraction enhanced imaging at NSLS and APS *Nucl. Instrum. Methods Phys. Res.* A submitted